A&A 628, A109 (2019)
https://doi.org/10.1051/0004-6361/201834892

Astronomy & Astrophysics

IMEM2: a meteoroid environment model for the inner solar system

R. H. Soja[1], E. Grün[2], P. Strub[1], M. Sommer[1], M. Millinger[3], J. Vaubaillon[4], W. Alius[1], G. Camodeca[1], F. Hein[1], J. Laskar[4], M. Gastineau[4], A. Fienga[4,5], G. J. Schwarzkopf[1], J. Herzog[1], K. Gutsche[1], N. Skuppin[1], and R. Srama[1]

[1] Institute of Space Systems, University of Stuttgart, Pfaffenwaldring 29, 70569 Stuttgart, Germany
e-mail: srama@irs.uni-stuttgart.de
[2] Max Planck Institute for Nuclear Physics (MPIK), Saupfercheckweg 1, 69117 Heidelberg, Germany
[3] ESTEC, Noordwijk, The Netherlands
[4] ASD/IMCCE, CNRS-UMR8028, Observatoire de Paris, PSL University, Sorbonne Université, 77 Avenue Denfert-Rochereau, 75014 Paris, France
e-mail: laskar@imcce.fr
[5] GéoAzur, CNRS-UMR7329, Observatoire de la Côte d'Azur, Université Nice Sophia Antipolis, 250 Av. A. Einstein, Valbonne 06560, France
e-mail: fienga@oca.eu

Received 15 December 2018 / Accepted 2 July 2019

ABSTRACT

Context. The interplanetary dust complex is currently understood to be largely the result of dust production from Jupiter-family comets, with contributions also from longer-period comets (Halley- and Oort-type) and collisionally produced asteroidal dust.
Aims. Here we develop a dynamical model of the interplanetary dust cloud from these source populations in order to develop a risk and hazard assessment tool for interplanetary meteoroids in the inner solar system.
Methods. The long-duration (1 Myr) integrations of dust grains from Jupiter-family and Halley-type comets and main belt asteroids were used to generate simulated distributions that were compared to COBE infrared data, meteor data, and the diameter distribution of lunar microcraters. This allowed the constraint of various model parameters.
Results. We present here the first attempt at generating a model that can simultaneously describe these sets of observations. Extended collisional lifetimes are found to be necessary for larger (radius > 150 μm) particles. The observations are best fit with a differential size distribution that is steep (slope = 5) for radii > 150 μm, and shallower (slope = 2) for smaller particles. At the Earth the model results in ~90–98% Jupiter-family comet meteoroids, and small contributions from asteroidal and Halley-type comet particles. In COBE data we find an approximately 80% contribution from Jupiter-family comet meteoroids and 20% from asteroidal particles. The resulting flux at the Earth is mostly within a factor of about two to three of published measurements.

Key words. meteorites, meteors, meteoroids – zodiacal dust

1. Introduction

The zodiacal dust cloud in the inner solar system consists of the ejection products of cometary outgassing and fragmentation, and asteroidal collisions (Sykes et al. 2004). The importance of a complete understanding of this meteoroid environment was recognised early on in the development of space flight technology: NASA meteoroid penetration experiments on the satellites Explorer XV1 and XXIII and Pegasus were used to characterise the near-Earth meteoroid risk to early missions (Naumann 1966; Cour-Palais 1969; Kessler 1970). Pioneer 8 and 9 (Berg & Richardson 1969; Berg & Gerloff 1971), Helios (Gruen et al. 1980), and HEOS-2 (Hoffmann et al. 1975a,b) data, as well as lunar microcrater counts (Morrison & Clanton 1979), provided further information that was used by Grün et al. (1985) to build a comprehensive model of the meteoroid flux at Earth orbit.

Divine (1993) developed a model of five dust populations defined by mass and orbital properties (eccentric, inclined, halo, core, and asteroidal), which describes the total flux and directional impact velocities of particles impacting spacecraft out to 20 AU. An update to this model by Staubach et al. (1997) included further Galileo and Ulysses data (Grün et al. 1995a,b) to refit the model, affecting mostly smaller (<10^{-13} kg) particles. Interstellar dust is represented as a monodirectional flow. These models are calibrated to fit the Grün et al. (1985) flux at Earth orbit.

At the beginning of the new millennium, NASA and ESA developed separate meteoroid environment models. NASA developed (and currently continues development on) the Meteoroid Engineering Model (MEM and updated version MEMR2), which uses dynamical models of cometary and asteroid particle orbits fitted to meteor orbit radar and in situ data (McNamara et al. 2004; Moorhead et al. 2015). Alternatively, ESA developed the Interplanetary Meteoroid Environment Model (IMEM), which models the orbits of particles from Jupiter-family comets (JFCs) and asteroids, and was fitted largely to in situ data and infrared brightness measurements (Dikarev et al. 2005). An interstellar population is also provided. Cometary and asteroidal populations are split into heavier ("collision dominated") and lighter ("Poynting-Robertson dominated") groups. This results in a discontinuity in the mass flux. Modelled meteor observations were not used because they were found to be inconsistent with modelled infrared data.

The goal of this project is the development of a dynamical engineering model of the dust component of the space environment using state-of-the-art knowledge of dust cloud constituents and their development under dynamical and physical effects. This is an ESA-funded project that is intended to be an improvement on the IMEM model and to remove its step-wise mass flux by fully integrating the dynamics of particles of radii 1 μm–1 cm. The model is built from knowledge of the orbital distributions of the dust parent bodies (cometary and asteroidal populations). Also, required are the gravitational and radiation forces that influence the trajectories of grains emitted from these objects, and their probability of collision with other dust particles. The model is designed to match dust observations as closely as possible, including infrared data from the Cosmic Background Explorer (COBE), lunar microcrater diameter counts, meteor orbit radar velocity and orbital element distributions, as well as the flux of dust particles at the Earth.

Here we describe the components and construction of the dynamical model (Sect. 2), the observational datasets used, and their individual fitting to the model (Sect. 3). Subsequently, we present the best-fit combination to all datasets (Sect. 4) and finally we discuss the implications and limitations of the model results (Sect. 5).

2. Modelling the long-term trajectories of cometary and asteroidal dust particles

The model is built by first integrating the orbits of cometary and asteroidal particle distributions over 1 Myr, including gravitational and solar radiation forces, as well as a simple collisional model. This provided us with the distribution of dust particles from different cometary and asteroidal sources within the inner solar system. This was achieved by:

1. integration over 1 Myr of the trajectories of particles released by JFCs and Halley-type comets (HTCs) and main belt asteroids;
2. removal of particles from the resulting trajectory distribution once their collisional lifetime is exhausted;
3. expansion of the orbits along angular orbital elements to fill the inner solar system;
4. comparison to observations in order to scale the model and weight different free model parameters;
5. execution of the final model at the Earth to compare to the flux at the Earth.

Particles were emitted from JFCs and Halley-type comets (HTCs), and main belt asteroids. The JFC distribution was that used by Nesvorný et al. (2010), originally derived by Levison & Duncan (1997), and the HTC distribution was that used by Nesvorný et al. (2010), which used an inclination distribution from Levison et al. (2006a). The main belt asteroid (AST) distribution was produced by selecting asteroids with magnitudes $H < 15$ (as this is considered a complete distribution, Gladman et al. 2009) and $a < 5$ AU (as this limits the asteroid population to the region of interest) from the Minor Planet Center (MPC) database as of April 2016. Only particles ejected on bound (eccentricity <1) orbits are used.

These parent-body orbital distributions were used to provide initial particle orbits. No ejection velocity was applied as the resulting dispersion is small compared to that caused by other gravitational and radiation forces over the long integration times. The argument of perihelion, longitude of the ascending node, and the mean anomaly were selected randomly. This generates a rotationally symmetric distribution about the ecliptic poles and describes a model in which the objects emit uniformly along their orbits. This models disruption rather than pure dust emission through sublimation of surface ices (Nesvorný et al. 2010 used both a uniform emission and a perihelion emission and found that the results were similar, but adopt the uniform emission to model disruption of JFCs). We selected 10 000 starting orbits from each population distribution, for each of the following particle radii: 1, 5, 12.5, 25, 50, 125, 250, 500 and 1250 μm. Particle radii 2.5, 5 and 10 mm were derived from the integrated orbits for 1.25 mm, but the collisional lifetimes for each size were applied. This is valid as long as these populations are for the most part collisionally evolved. Bulk densities were 1000 kg m^{-3} for HTC particles, 2000 kg m^{-3} for JFC particles, and 4000 kg m^{-3} for AST particles.

The initial particle orbits were integrated for 1 Myr using the "PIntegrator", which uses a Runge-Kutta-Nyström 7(6) method with variable step size (Dormand & Prince 1978) to propagate the trajectories of all dust particles under solar and planetary gravity; radiation pressure; and Poynting-Robertson drag force, with a factor also included for solar wind drag (Soja et al. 2015). Particles that came within ten solar radii of the Sun were removed to manage the integration process and because particles inward of this distance are expected to sublimate (Mann et al. 2011). We used pre-calculated 1 Myr planetary ephemerides INPOP13c_LT (see Sect. 2.1 below), which span a time range from 1 Jan 498 000 BC to 1 Jan 502 000. Use of these ephemerides helped computationally, as then only the particles needed to be separately integrated. The end result was time-resolved particle states from the four source populations describing their trajectories over 1 Myr in time-steps of approximately 500 yr. It was assumed that every time-step along the particle trajectories is equally valid at the present time, thus simulating continuous emission of particles.

To obtain sufficient particle numbers these orbits were expanded by randomising the mean longitude, longitude of the ascending node, and longitude of perihelion. A total number of orbits N_{expand} was created for each trajectory point, which was typically between 10 and 1000, and is chosen to keep the datasets to under 4 GB. The collisional behaviour of particles was also implemented at this step. This probability is compared to a random value between zero and one for each particle at each step on its trajectory. Whenever the collisional probability for a given particle was higher than this random value, the orbit was removed from further time bins. This was evaluated separately for each expanded particle and therefore repeated N_{expand} times per trajectory. This resulted in a large set of particle states describing the dust cloud in the inner solar system (within $X, Y, Z = -6$ to $+6$ AU), for each mass and population.

We use a simple differential size distribution, fit by two slopes α and β for radii above and below a mid-point D_{mid}, as described by Pokorný et al. (2014). This size distribution is applied at the particle source. The ranges of α, β, and D_{mid} are motivated by previous studies (such as Pokorný et al. 2014): $\alpha = 2, 3, 4, 5$, $\beta = 1, 2, 3, 4$, $D_{\mathrm{mid}} = 50, 100, 150, 200\,\mu$m. It is also assumed that all populations have the same size distribution. This may not be valid for particles that originate in very different processes (such as asteroid break up or cometary activity). However, we made this assumption to restrict the number of fitting parameters.

The 1 Myr integration time may not be sufficient for the HTC population (Pokorný et al. 2014). However, our effort is limited by our computational resources, and based on previous studies we expect the JFC population to be dominant (e.g. Nesvorný et al. 2010).

2.1. The INPOP13c_LT planetary ephemerides

The INPOP ephemerides are highly accurate planetary ephemerides of the eight planets of our solar system but also of Pluto and the Moon. They are obtained by numerically integrating the barycentric Einstein-Infeld-Hoffmann equations of motion (Moyer 1971) in a suitable relativistic time-scale and take into account more than 100 asteroids of the main belt. Since the publication by Fienga et al. (2008), the INPOP planetary ephemerides have been regularly improved (Fienga et al. 2009, 2010, 2011, 2015; Viswanathan et al. 2018).

In the present work, we use a special version of the INPOP13c ephemerides (Fienga et al. 2015) that has been tailored for use over long time periods. The INPOP13c ephemerides are built over the whole sample of modern and ancient planetary observations from ten years of the Cassini round-trip around Saturn and its system up to the first photographic plates of Pluto. Despite some differences in the dynamical modelling and in fitting choices, as described in Fienga et al. (2015), INPOP13c is very close to the JPL DE430 planetary ephemerides (Folkner et al. 2014).

In order to overcome the time limitations that exist in usual precision ephemerides, we removed all elements that would directly limit the length of validity of the solutions from the construction of the INPOP ephemerides. In particular, we did not use some precession formulas for the evolution of the spin axis of the Earth. Instead, we integrated, together with the full ephemeris, a precession model for the Earth that is obtained after averaging over the rotation period of the Earth (Fienga et al. 2008).

The full ephemeris is then prolonged over 1 Myr (−500 kyr to +500 kyr) using extended precision 80-bit arithmetics with the Adams integrator of INPOP. For this long-time solution that is referred to here as INPOP13c_LT, we made a few modifications with respect to the published version of INPOP13c[1]. In particular, although 137 asteroids are taken into account as in INPOP13c, the additional asteroid ring, taking into account all remaining asteroids in an averaged manner, is not present in INPOP13c_LT. The secular variation of the Earth flattening coefficient J_2 due to the glacial rebound is not taken into account, as it becomes meaningless over such a long time. In the same way, the dissipation in the libration of the Moon has been suppressed. Due to these changes, a readjustment of the initial conditions of the Moon, and a fit of the Earth tidal parameters τ_{21} and τ_{22} has been performed, such that the solutions INPOP13c_LT fits with INPOP13c over its range.

The numerical integration is performed with a step-size of about 0.05534 days with an output every 100 steps. This output is then extrapolated using Tchebychev polynomial interpolation. The differences between INPOP13c and INPOP13c_LT over the whole range of INPOP13c (+1000 to +3000 AD) are less than 1 m for the planets and 34 m for the Moon. This is much less than the estimate of the uncertainty of the solution (see Fienga et al. 2014). The Tchebychev polynomial representation provides an interpolation precision of about 350 km for each planet over the whole range of INPOP13c_LT.

2.2. Collisions model

The collisional lifetime of a meteoroid is dependent on the characteristics of the meteoroid itself, as well as the number and speed of projectile particles in interplanetary space that are capable of collisionally destroying the target meteoroid. We calculated the collisional lifetime from the rate of catastrophic collisions (collisions in which largest collisional fragment is half the size of the original target particle), under the assumption that the meteoroid is destroyed by the smallest particle able to do so.

The size of the projectile able to catastrophically fragment a meteoroid was calculated using the formalism of Grün et al. (1985). The target meteoroid (mass m_1) is disrupted by a particle of mass m_2 when $m_1 \leq \Gamma m_2$, where Γ is derived using the results of Gault (1973) and Hoerz et al. (1975b) for crystalline rock:

$$\Gamma = 9.76 \times 10^2 S_c^{-0.45} (m_1/\rho_1)^{0.075} v^2,$$

where ρ_1 (g cm^{-3}) is the target meteoroid density, $S_c = 3$ (kbar) is the unconfined compressive strength, and v (km s^{-1}) is the impact speed.

This provided the mass of a particle that can catastrophically disrupt the target meteoroid for a given impact velocity. The collisional probability was calculated by determining the number of particles with greater mass than this that impact the meteoroid. The projectile particle flux and impact velocity information was extracted from the IMEM model (Dikarev et al. 2005). This means that our model is partially dependent on the original IMEM model: a more consistent approach would require iteration of the collisional model until a steady state is achieved. However, this is computationally intensive and is therefore the subject of a future study.

This allowed us to calculate the collisional lifetime along any orbit (perihelion distance, eccentricity, and inclination) in the inner solar system. The collisional lifetime along a given orbit was determined by combining the collisional probability at 100 points along one orbit of the meteoroid. This gave us sufficient resolution to fully sample the collisional behaviour along one orbit. This describes the collisional lifetime of a specific object only when the orbit is stable. Within the current model, this information was therefore updated approximately every 500 yr. The collisional lifetimes at Earth orbit are in good agreement with the results of Grün et al. (1985), except for a small deviation at high velocities that is a result of the difference in the impact velocities between our dynamical model and the 20 km s^{-1} assumed by Grün et al. (1985).

We developed a database of collisional lifetimes for test particles with different combinations of orbital elements: a range of perihelion distances between 0 and 6 AU, eccentricities of 0–0.9, and inclinations of 0–180° (a slight dependency on the argument of perihelion is not considered and could be included in further investigations). Each point along the integrated orbits described above was assigned a collisional lifetime equal to the closest orbit in the database. Orbits that exceed an aphelion distance of $Q = 40$ AU reach beyond the outer limit of the IMEM model and are assigned linearly extrapolated values, based on the eccentricity behaviour, which is generally stable. The collisional lifetime is used to derive the collisional probability $p = 1 - \exp(\frac{-dt}{\tau_{\rm coll}})$ using the time-step $\tau_{\rm coll}$, as in Nesvorný et al. (2011b) and Pokorný et al. (2014). Figure 1 shows collisional lifetimes as a function of mass for a selection of comet and asteroid orbits, as well as an Earth orbit.

Basalt was used for the original experiments on which the calculation of Γ are based. The composition and material structure of meteoroids likely behaves differently in collisions. There is therefore a high uncertainty on the calculated collisional lifetimes. Additionally, a requirement for higher collisional lifetimes was suggested by previous studies (Nesvorný et al. 2010, 2011a;

[1] https://www.imcce.fr/inpop/

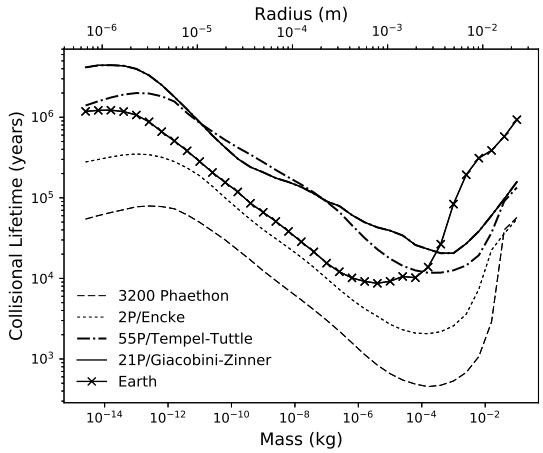

Fig. 1. Collisional lifetimes as a function of mass along the trajectories of different solar-system objects.

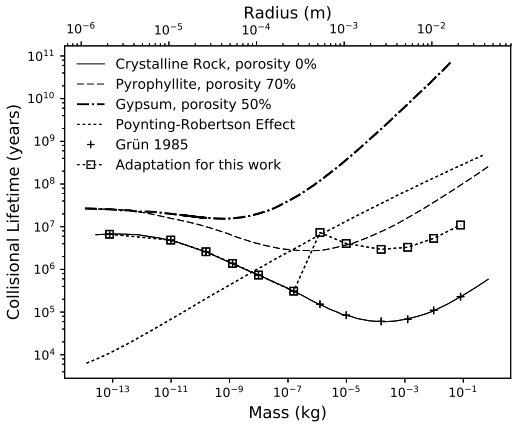

Fig. 2. Comparison of collisional lifetimes for different materials and porosities. The solid line represents the original Grün et al. (1985) lifetimes: crosses demonstrate the particle sizes used in this model. The squares provide these collisional lifetimes when multiplied by the $F_{\rm coll}$ given in Table 1, which varies with particle size. This is compared to recalculations of the collisional lifetimes using the method of Grün et al. (1985), but using the experimental results of Nakamura et al. (2015), which demonstrate how they are variable with particle material and porosity (dashed and dot-dashed lines). Finally, the Poynting-Robertson lifetimes (dotted line) demonstrate how the dominance of Poynting-Roberston drag or collisional shattering is dependent on particle composition and structure.

Table 1. Example of variation of the collisional lifetime scaling factor $F_{\rm coll}$ per particle radius (s).

$s(\mu$m)	1	5	12.5	25	50	125	250	500	1250	2500	5000	10000
$F_{\rm coll}$	1	1	1	1	1	1	50	50	50	50	50	50

Pokorný et al. 2014). We therefore varied the collisional lifetime using a factor $F_{\rm coll}$, as employed by Pokorný et al. (2014).

Furthermore, these studies also suggest that this collisional factor may not be the same for all particle sizes, and may increase with particle size (Nesvorný et al. 2011a). We therefore also test the case in which $F_{\rm coll}$ is defined separately for each particle size in the range 1 μm–1 cm. An example is given in Table 1, which is later used for the model fitting. This is a simplified approach, taken because we have insufficient observational constraints to fit $F_{\rm coll}$ as a continuous function of particle radius. Likely, the variation in particle collisional behaviour is a result of the chemical and structural composition of meteoroids. For instance, new experimental results with a range of materials (crystalline rock, gypsum, and pyrophyllite) demonstrate that reduced porosity can increase the collisional lifetime of dust particles in interplanetary space (Love et al. 1993; Nakamura et al. 1994, 2015), especially for larger meteoroids. Figure 2 uses the results of Nakamura et al. (2015) to recalculate the collisional lifetimes given in Grün et al. (1985) for different materials and porosities. This is compared to the Grün et al. (1985) collisional lifetimes after applying the variable $F_{\rm coll}$ in Table 1. We conclude that such a set of size-dependent $F_{\rm coll}$ is physically reasonable. The model however does not explicitly use the collisional lifetimes derived using Nakamura et al. (2015) because porosity is not included in the particle dynamics.

Finally, our model does not consider more than the first generation of collisions: particles that collide catastrophically are removed from the simulation and do not generate fragments. This, along with an iteration of the collisional model to remove reliance on the original IMEM velocities and meteoroid fluxes, would be important next steps for such modelling.

3. Observations

These simulations provided us with trajectory information for JFC, HTC, and AST particles. These modelled particles were then used to calculate infrared brightness profiles to compare with COBE data (Sect. 3.1); the lunar microcrater diameter distribution (Sect. 3.2); meteor radar orbit and velocity distributions (Sect. 3.3); and the cumulative flux distribution at the Earth (Sect. 3.4). The optimal combination of model parameters was chosen by varying the mass distribution parameters α, β, and $D_{\rm mid}$, the collisional lifetime factor $F_{\rm coll}$, and the scaling factors for each population, $S_{\rm JFC}$, $S_{\rm HTC}$, and $S_{\rm AST}$. Here the assessment of the optimal fits is done qualitatively. Quantitative fits to the COBE data are given in Sect. 4.

3.1. COBE infrared data

The infrared sky is dominated by the interplanetary dust cloud at some wavelengths. For observations from the Cosmic Background Explorer (COBE), primarily designed to characterise the cosmic microwave background, the 25 μm wavelength is optimal for extraction of the interplanetary dust signature, although important signatures are found also in 4.9, 12, and 60 μm. The COBE interplanetary dust component was characterised by Kelsall et al. (1998). We compared the latitudinal profiles at a solar longitude of 90° derived from COBE data and from the modelled dust trajectories, using the infrared brightness per pixel from COBE DIRBE weekly data files at 25 μm. Galactic contamination was avoided by removing pixels within 10° of the galactic plane and by averaging over weeks in which the galactic contamination is far from the ecliptic plane. We needed to adjust for a small offset from the centre (~2°), which is likely caused by asteroid bands, in order to compare our model with this data (see, e.g. Nesvorný et al. 2010).

The modelled dust trajectories were used to generate a sky brightness latitudinal profile at 25 μm for a solar longitude of 90°. The brightness contribution for each particles was calculated using Planck's law and assuming a temperature $T(K) = 280 \times r_{\rm h}^{-0.5}$, where $r_{\rm h}$ is the heliocentric distance of the particle (see Nesvorný et al. 2010).

The infrared data strongly suggest that JFCs are the dominant contributor to the interplanetary dust cloud (Fig. 3). The

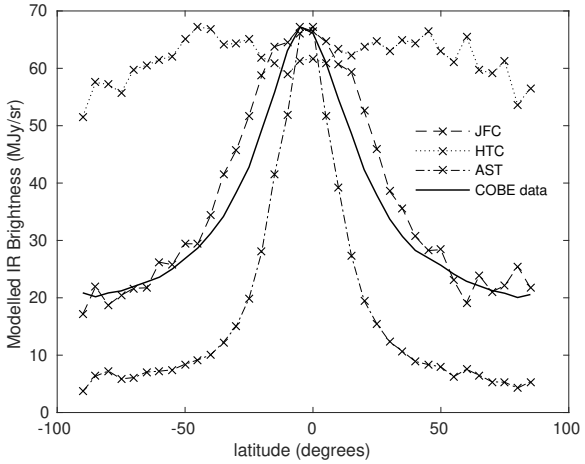

Fig. 3. Modelled infrared brightness profiles for JFCs, HTCs, and ASTs compared to the COBE 25 μm brightness profile at a solar longitude of 90°. $F_{\rm coll} = 1$, mass distribution $\alpha = 5, \beta = 2, D_{\rm mid} = 200\ \mu$m.

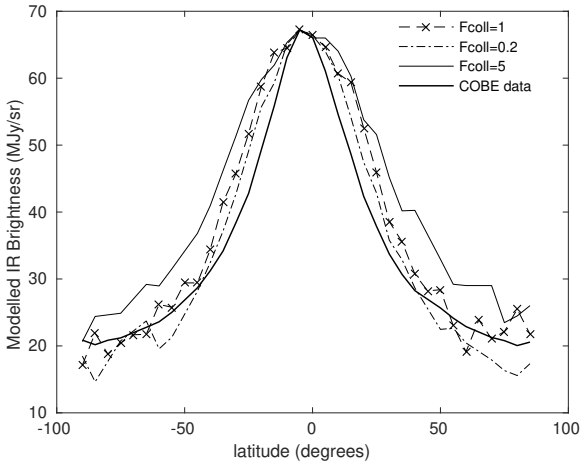

Fig. 4. Modelled infrared brightness profiles for JFCs for $F_{\rm coll} = 1$, 0.2, and 5, compared to the COBE 25 μm brightness profile at a solar longitude of 90°. Mass distribution $\alpha = 5, \beta = 2, D_{\rm mid} = 200\ \mu$m.

high inclinations of the HTC population result in a wide brightness profile. Conversely, the infrared profile for the AST source, which is largely limited to the ecliptic plane, is narrow. Our JFC profile is slightly wider than the COBE profile, in contrast to the results of Nesvorný et al. (2011a). This may be a result of the differences in the collisional lifetimes used, in particular with regard to the dependence of the collisional lifetime on orbital elements. An improved fit between the data and the JFC model profile is achieved by shortening the collisional lifetime (Fig. 4). The infrared brightness is not strongly affected by the mass distribution.

3.2. The lunar microcrater number distribution

The distribution of microcraters on the moon provides valuable information on the distribution of meteoroids in near Earth space (Grün et al. 1985). Hoerz et al. (1975a) reported the lunar crater pit diameter $D_{\rm pit}$ as described by $D_{\rm pit} = cm^{\lambda}$, where c and λ are constants dependent on the projectile properties and the effective impact velocity v, and m is the particle mass in grams. For a bulk density $\rho = 3000$ kg m^{-3} and an impact speed of 20 km s^{-1} they found $c = 8.24$ and $\lambda = 0.370$. When the velocity factor is extracted this provides: $D_{\rm pit} = 2.06 \times 10^{-2} v^2 m^{0.37}$.

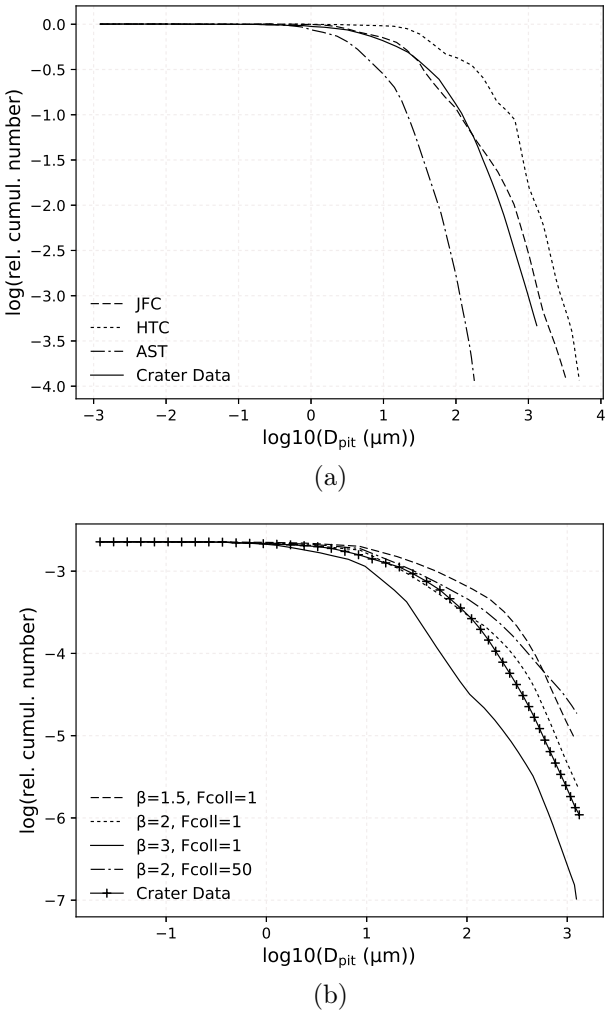

Fig. 5. Modelled lunar crater distribution for (*a*) $F_{\rm coll} = 1$ and JFC, HTC and AST, and (*b*) JFC for variations in β and $F_{\rm coll}$ with $\alpha = 5$, and $D_{\rm mid} = 200\ \mu$m.

We used this formula to construct a crater diameter number distribution for the dust model. This was compared to the large crater part of the lunar crater distribution of Morrison & Clanton (1979), which represents meteoroids. The lower-mass section of the crater distribution is a result of beta meteoroids and lunar ejecta, which are not considered in this model (Grün et al. 1985). A solution with a large component of JFC particles and $F_{\rm coll} = 1$ is most consistent with the data (Fig. 5). The lunar crater diameter distribution is also sensitive to the mass distribution: $\alpha = 5$, $\beta = 2$, and $D_{\rm mid} = 100 \times 10^{-6}$ m provides the best fit. This data provides a constraint on β (Fig. 5b). However, the interpretation of the lunar microcrater distribution is dependent on the accuracy of the conversion from craters to the meteoroid population, similarly to the calculation of the collisional lifetimes as described in Sect. 2.2. To simplify the fitting process we assume that the distribution is valid; a future study should analyse the affect of different crater models on the fitting.

3.3. Meteors

Meteor observations from Earth provide the most complete set of orbital information for interplanetary dust at 1 AU. The Advanced Meteor Orbit Radar (AMOR), which was operated in Christchurch, New Zealand, was sensitive to meteors down to approximately +14 radar magnitude. The Canadian Meteor Orbit

Radar (CMOR) in Ontario detects larger meteors, with a limiting magnitude around +8. These two systems therefore allow us to test the operation of the model at two different size regimes.

The distribution of meteors at the Earth is dominated by six "sporadic sources", which describe concentrations in radiant space that do not necessarily correspond to physical sources of meteoroids. We therefore describe them as "categories" in order to distinguish them from cometary and asteroids dust sources. The helion and anti-helion categories are usually the strongest sources and are found in the ecliptic plane at 70° from the apex direction. The north and south apex categories are found in the direction of the Earth's motion, and at ecliptic latitude ~±20° (Hawkins 1956; Weiss & Smith 1960; Jones & Brown 1993). The north and south toroidal categories are located 60° north and south of the apex direction (Hawkins 1962, 1963; Jones & Brown 1993). Bias-corrected impact speed and orbital element distributions (semi-major axis, eccentricity, and inclination) for these sporadic sources are provided by Galligan & Baggaley (2005) and Campbell-Brown (2008) for AMOR and CMOR, respectively.

We identified particles within a $\sim 0.09 \times 0.09 \times 0.06$ AU box centered at the Earth and converted these particle states to orbits. We applied different ionisation limits to simulate the particle distribution that is observed by different radar systems, as in Wiegert et al. (2009) and Nesvorný et al. (2011a). Particles were considered detectable if they have $I(m, v) = (m/10^{-4})(v/30)^{3.5}$ greater than a set cutoff $I_{\rm limit}$, which is dependent on the radar system: $I(m, v) \geq I_{\rm limit}$. The limiting magnitude of the AMOR system approximately corresponds to $I_{\rm limit} = 0.01$, while $I_{\rm limit} = 1$ is representative of the CMOR limiting magnitude (Galligan & Baggaley 2005; Campbell-Brown 2008). We corrected for the flux at Earth, and for the impact speed we also corrected for the zenith attraction. We then extracted separately helion, apex, and toroidal category particles.

Jupiter-family comet meteoroids populate the helion category (Fig. 6). Helion meteoroids were selected within latitude b and longitude l (centred on the Earth Apex direction) with $l = \pm 30$–$120°$ and no latitude restriction for AMOR, and $l = \pm 45$–$120°$ and $b = -30$ to $+30°$ for CMOR. Although they detect particles of different sizes, the AMOR and CMOR orbital element and velocity distributions are similar. This was interpreted by Nesvorný et al. (2011a) as an indication that meteoroids have different collisional behaviour – AMOR meteoroids require no enhancement of the collisional lifetime, while CMOR meteoroids require an enhancement of $F_{\rm coll} = 50$–100. We confirm that while the orbital element distributions for AMOR meteoroids (radius ~50 μm in the helion category) require $F_{\rm coll} = 1$–5, CMOR meteoroids (radius 250 μm) need $F_{\rm coll} = 30$–50. This is consistent with the infrared brightness, which is dominated by particles of 25–50 μm in size, and requires low collisional lifetimes. The width of the velocity distributions can be changed by altering the mass distribution.

The apex category – consisting of particles that impact the Earth head on – requires a longer-period comet source to match the retrograde orbits. This has previously been modelled as a long-period comet source (Wiegert et al. 2009; Nesvorný et al. 2011b). Here we investigate whether our HTC population can function as such a source. Apex meteoroids were selected within $l = -21$ to $+21°$ and $b = -30$ to $+30°$. Figure 7 demonstrates the variation in the orbital distributions as $F_{\rm coll}$ is increased. Using $F_{\rm coll} = 10$–50 produces near identical results. The limitation of an integration time of only 1 Myr is that it prevents these particles from evolving for sufficiently long timescales to truly represent $F_{\rm coll} > 10$. The HTC population may indeed be a strong

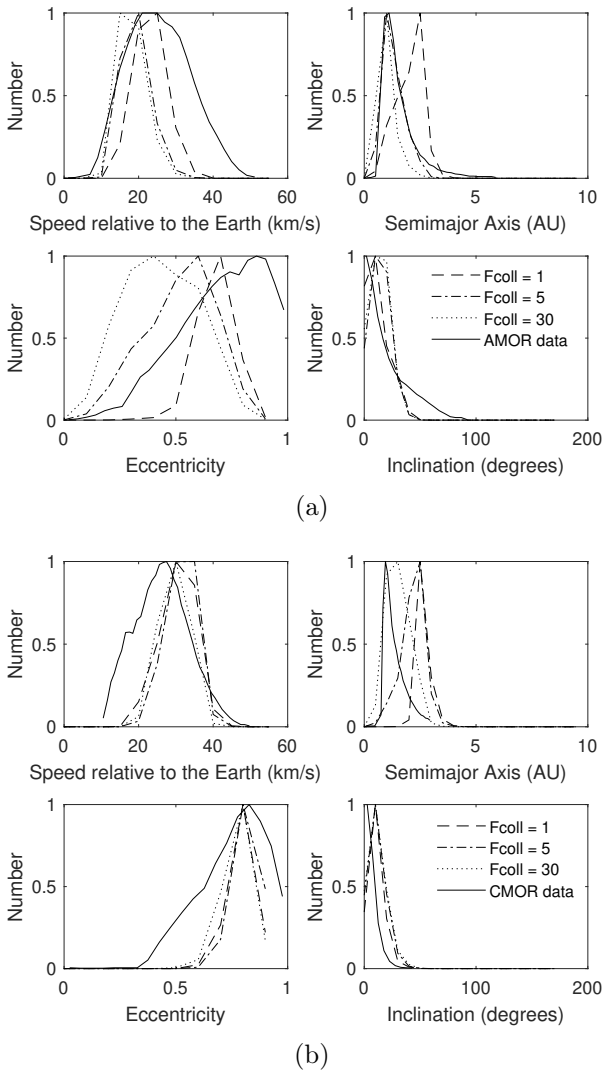

Fig. 6. Modelled impact speed and orbital elements at Earth for JFC meteoroids for the helion category, compared to AMOR (*a*) and CMOR (*b*) data, for $F_{\rm coll} = 1$, 5, and 30, and mass distribution $\alpha = 5$, $\beta = 2$, and $D_{\rm mid} = 200$ μm.

contributor to the apex category, but this would have to be further tested with longer integration times. Furthermore, the contribution of long-lived Oort-cloud comet particles, as calculated by Nesvorný et al. (2011b), should also be investigated.

Similar behaviour is seen for the toroidal category. Toroidal meteoroids were selected within $l = -15$ to $+15°$ and $b = \pm 48$–$60°$. The model velocity, eccentricity, and inclination decrease as $F_{\rm coll}$ increases (Fig. 8). However, this is still insufficient to achieve a good fit to the CMOR data. This is again likely a consequence of the 1 Myr limit on the integrations: there is only a very small difference between the orbital distributions for $F_{\rm coll} = 20$ and $F_{\rm coll} = 50$. Moreover, Pokorný et al. (2014) require several million years of integration of HTC meteoroids to match CMOR observations of the toroidal category with $F_{\rm coll} \approx 20$.

Integrations over 5–20 Myr are expected to significantly improve the fit between meteor data and the model orbital distributions. However, the CMOR apex and toroidal distributions have a binary form that could be evidence of the contribution of two parent populations to the distribution. At first glance, it appears that the orbital elements of JFC and AST meteoroids

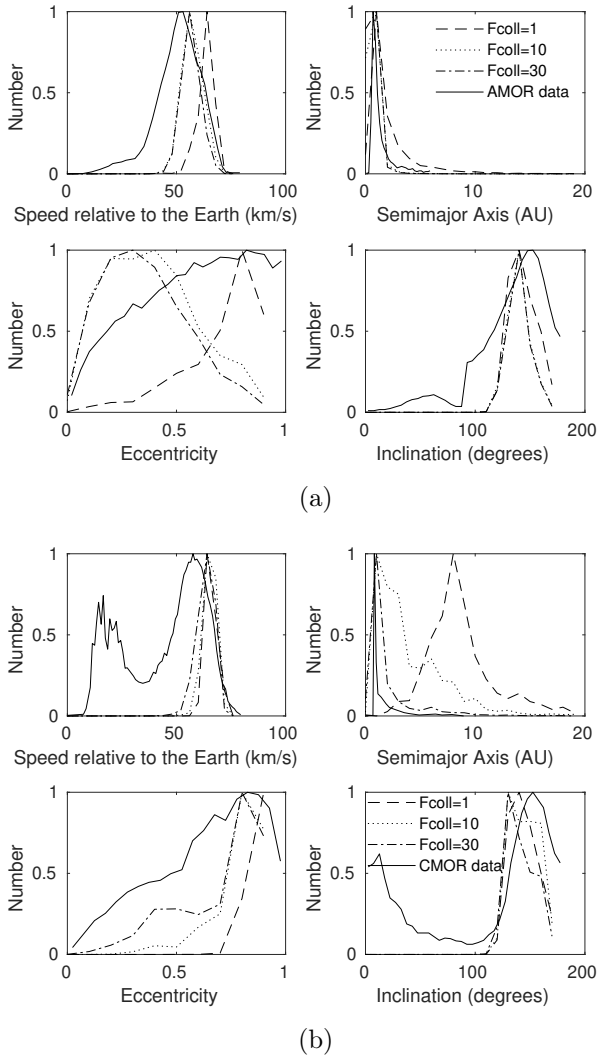

Fig. 7. Modelled impact speed and orbital elements at Earth of HTC meteoroids for the apex category, compared to AMOR (*a*) and CMOR (*b*) data, for $F_{\rm coll} = 1$, 10, and 30, and mass distribution $\alpha = 5$, $\beta = 2$, and $D_{\rm mid} = 200\ \mu$m.

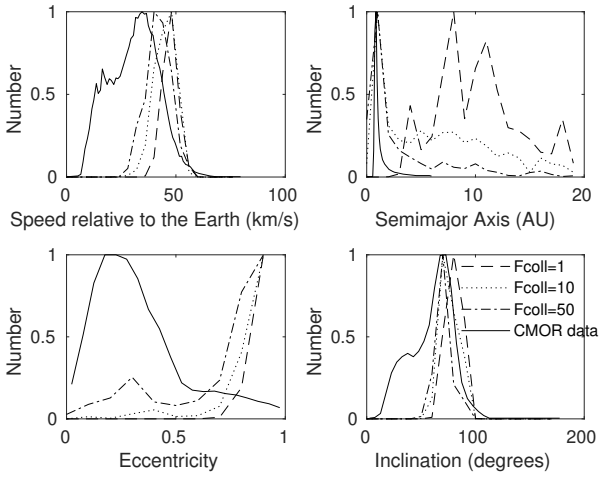

Fig. 8. Modelled impact speed and orbital elements at Earth of HTC meteoroids for the toroidal categories, compared to CMOR data, for $F_{\rm coll} = 1$, 10, and 30, and mass distribution $\alpha = 5$, $\beta = 2$, and $D_{\rm mid} = 200\ \mu$m.

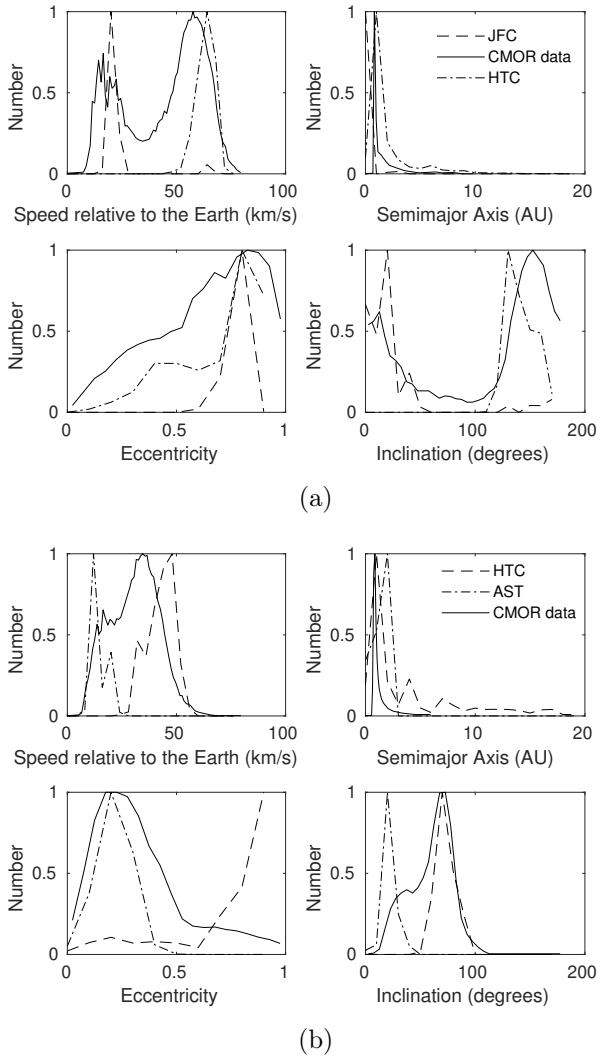

Fig. 9. Modelled impact speed and orbital elements at Earth for the apex (*a*) and toroidal (*b*) categories, compared to CMOR data, for $F_{\rm coll} = 30$ and mass distribution $\alpha = 5$, $\beta = 2$, and $D_{\rm mid} = 100\ \mu$m.

may partially contribute to the apex and toroidal orbital distributions, respectively (Fig. 9). However, this would require large proportions of JFC particles that would oversaturate the helion/anti-helion. Furthermore, the particle numbers are too low to scale the different populations contributing to each radiant category. Additionally, this secondary population at lower velocities does not appear in the AMOR apex category, even though we would expect more of these lower-speed particles to be visible in the AMOR dataset. The toroidal category is also extracted by Janches et al. (2015) from SAAMER radar data: this demonstrates a stronger lower-velocity component and suggests a dimorphism between the north and south toroidal categories that is not present in the structure of our model.

3.4. Flux distribution at Earth

The flux distribution describes the actual number of particles predicted by the model to impact the orbit of Earth. Grün et al. (1985) use a variety of observations to construct a flux curve for dust at the Earth, including in the small beta-meteoroid size range that is not covered by this model. The Grün et al. (1985) flux is scaled at intermediate particle sizes to the Pegasus; meteor

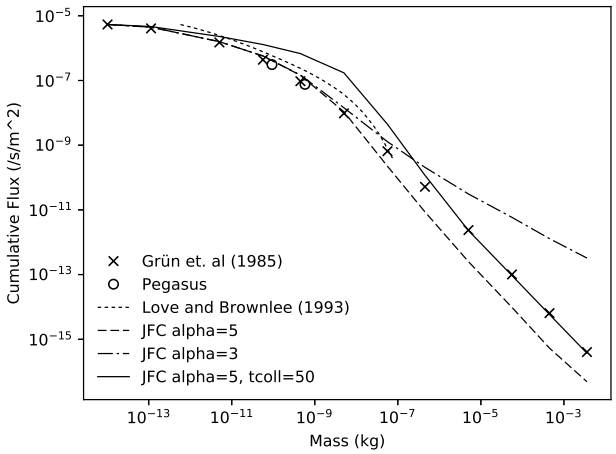

(a)

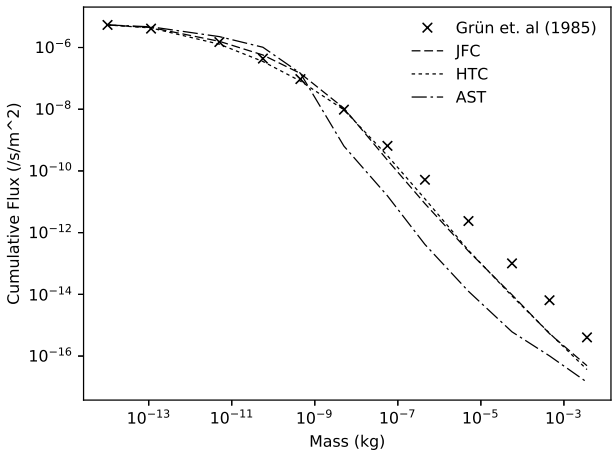

(b)

Fig. 10. Flux model compared to distributions from Grün et al. (1985) and Love & Brownlee (1993). (*a*) For JFC, $F_{\rm coll} = 1$ and 50 with $\alpha = 5$, $\beta = 2$, $D_{\rm mid} = 200$ μm, and also demonstrating the effect of changing $\alpha = 5$ to $\alpha = 3$. (*b*) For JFC, HTC and AST, with $F_{\rm coll} = 1$ and $\alpha = 5$, $\beta = 2$, $D_{\rm mid} = 200$ μm.

observations are used at high masses. Additionally, Love & Brownlee (1993) use impact craters on the Long Duration Exposure Facility (LDEF) to calculate a flux that is around two times higher than the Pegasus measurements. Borin et al. (2011) use hydrocode simulations to rescale the LDEF flux for cometary and asteroid populations: the flux is then consistent with the results of Grün et al. (1985) for masses of 10^{-12}–10^{-14} kg. We therefore usually compare our flux to the Grün et al. (1985) results.

We calculated the interplanetary flux at the Earth for a variety of populations, $F_{\rm coll}$, and mass distributions and compared this to the Grün et al. (1985) and Love & Brownlee (1993) data (Fig. 10). We calculated the flux directly from the number and velocity of particles within ±0.05 AU of the orbit of Earth, and then corrected for flux on to a flat plate as described in Grün et al. (1985). The flux in Love & Brownlee (1993) requires a correction to an interplanetary flux, also as described in Grün et al. (1985). This distribution provided a constraint on α of the mass distribution because a larger slope ($\alpha = 5$) is strongly favoured (Fig. 10a). $F_{\rm coll} = 1$ is also preferred.

4. Combination of observations

We now search for a combination of particle population weighting and the parameters $F_{\rm coll}$, α, β, and $D_{\rm mid}$ that best describes all observations. The individual observations described in Sect. 3 provide the following constraints:

– From the infrared distribution it is required that JFC meteoroids are dominant, but also that there is a moderate level of asteroidal particles or another low-inclination source such as Encke-type comets (Fig. 3). A large contribution of Encke-type comets is supported by Wiegert et al. (2009). A low level of HTC particles is required for the meteor observations (Figs. 7 and 8).

– $F_{\rm coll} \leq 1$ is likely needed for ~50 μm particles for the infrared brightness profile (Fig. 4; although a small AST component may allow a larger range of solutions) and $F_{\rm coll} \geq 1$ is required for AMOR-sized meteoroids (Fig. 6). Lunar microcraters have the best fits for these sizes with $F_{\rm coll} = 1$.

– $F_{\rm coll} = 30$ or 50 is required for CMOR-sized meteoroids (Fig. 6). The apex and toroidal categories also suggest that a high $F_{\rm coll}$ is required, but this cannot be constrained further because of the 1 Myr limit in the dynamical evolution of released particles (Figs. 7 and 8).

– $\beta = 2$ is required for the lunar microcrater distribution. Lower β resulted in an excess of craters while higher β resulted in too few craters (Fig. 5).

– $\alpha = 5$ is required for the flux distribution at Earth. Lower α resulted in an excess in the flux at higher masses (Fig. 10).

We still need to specify exact population weightings for each of JFC, HTC, and AST; choose a $D_{\rm mid}$; and decide between various options for the collisional lifetime. The population weightings are automatically selected by calculating the best fit to the COBE infrared brightness data using the normalised root-mean-square error. For most solutions presented here the goodness of fit is optimised for 80% JFC, 0.5% HTC, and 19.5% AST. Although there also exists a small number of solutions with higher proportions of AST and HTC that can combine to provide a good fit, these are not further considered because the initial good fit of the JFC distribution alone makes this the more likely dominant population.

Better crater fits are achieved for $D_{\rm mid} = 100$ μm, but better infrared profile fits are found for $D_{\rm mid} = 200$ μm. We therefore selected an intermediate $D_{\rm mid} = 150 \times 10^{-6}$ m that provides us with a goodness of fit of greater than 0.8 for both lunar craters and the infrared profile. This is dependent on the $F_{\rm coll}$ and generally falls between $D_{\rm mid} = 110$ μm and $D_{\rm mid} = 160$ μm.

The exact choice of $F_{\rm coll}$ is not well constrained. We start with an array $F_{\rm coll} = [1\ 1\ 1\ 1\ 1\ 1\ 50\ 50\ 50\ 50\ 50\ 50]$, meaning that particle sizes 1–125 μm have $F_{\rm coll} = 1$ and sizes 250 μm–1 cm have $F_{\rm coll} = 50$ (as discussed in Sect. 2.2). If we instead choose $F_{\rm coll} = 50$ for 125 μm particles also, the fitting to the infrared data requires a low $D_{\rm mid} = 5$ μm, which does not provide a good fit for the lunar microcraters. Using $F_{\rm coll} = 30$ for 125 μm particles however does not produce this affect. $F_{\rm coll} = [1\ 1\ 1\ 1\ 1\ 1\ 30\ 50\ 50\ 50\ 50\ 50]$ does not provide significantly different fits and is not considered further. The effect of using $F_{\rm coll} = 30$ for all higher masses is also similar but since the fits for toroidal and apex meteors are slightly worse, we favour $F_{\rm coll} = 50$ for the highest masses. We are therefore left with the two options $F_{\rm coll} = [1\ 1\ 1\ 1\ 1\ 1\ 50\ 50\ 50\ 50\ 50\ 50]$ and $F_{\rm coll} = [1\ 1\ 1\ 1\ 1\ 30\ 50\ 50\ 50\ 50\ 50\ 50]$.

Absolute scaling of the model (with its initial 10 000 test particles per population, expanded to fill the dust cube) to the data is carried out using the infrared data, which is considered to

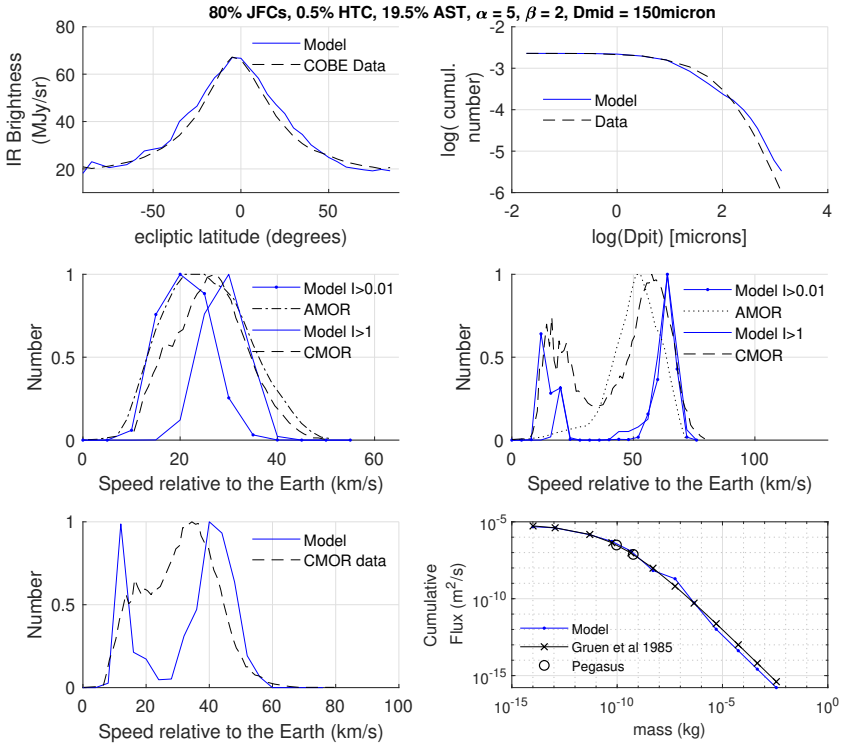

Fig. 11. Summary of fit between observational datasets and the model for COBE data (*a*) and the lunar microcrater number distribution (*b*), and meteor data for the helion (*c*), apex (*d*), and toroidal (*e*) categories. Finally, a comparison is shown between the cumulative flux (spinning plate) at Earth for this model and from Grün et al. (1985) (*f*). Population weighting 80% JFC, 0.5% HTC, and 19.5% JFC. $F_{\rm coll}$ = [1 1 1 1 1 1 50 50 50 50 50 50]. Mass distribution $\alpha = 5, \beta = 2, D_{\rm mid} = 150\,\mu$m.

Table 2. Final model parameters.

Parameter	Value
$F_{\rm coll}$ per size	1 1 1 1 1 1 50 50 50 50 50 50
α, β, $D_{\rm mid}$	5, 2, 150×10^{-6} m
JFC/HTC/AST scaling	$4.0 \times 10^{+20}$ 2.4×10^{19} 7.8×10^{18}

be the most accurate quantitative information. This results in a scaling factor which represents the number of real particles represented by each test particle in the model, for JFC, HTC, and AST particles, respectively (see Table 2 for an example).

When these factors are applied to the flux at the Earth, which is our only other quantitative measurement of the dust cloud, the result is similar to the flux reported by Grün et al. (1985). At smaller masses there is a good fit between the model and the measured flux (factor 0.9–1.3). At the knee there is a difference of a factor of three. At larger masses our flux is about 0.4 of the Grün et al. (1985) flux. Given that the results of Borin et al. (2011) suggest that the LDEF flux may agree more closely with the Pegasus flux, higher measurement uncertainties are expected within the meteor-sized particle regime. At larger masses the flux is constrained by meteor data that is highly dependent on the poorly known luminous efficiency. Koschny et al. (2017) derive the mass flux from meteoroids detected by the Canary Island Long-Baseline Observatory (CILBO). They show that although the luminous efficiency derived by Weryk & Brown (2013) leads to a good fit to the Grün et al. (1985) flux, that derived by Verniani (1965) gives an order of magnitude more flux. There are therefore good reasons to suspect that these flux measurements at the Earth contain some uncertainty, particularly for larger particle sizes.

Finally, we select the option with $F_{\rm coll}$ = [1 1 1 1 1 1 50 50 50 50 50 50] (Fig. 11) due to small advantages in the flux, which has less of a strong knee and has a lower maximum difference to Grün et al. (1985) and AMOR helion meteor distributions. The final choice is given in Table 2. There are several possibilities that would improve the individual fits to the infrared brightness profile, lunar microcrater diameter distribution, or meteor orbital data individually. Nonetheless a singular solution is required for the meteoroid environment model. Figures 12 and 13 provide further information on the meteor orbital distributions for this set of parameters.

In Fig. 14 we compare the modelled flux to the original IMEM model (Dikarev et al. 2005) and MEMR2 (McNamara et al. 2004; Moorhead et al. 2015). IMEM is fit to the Grün et al. (1985) at lower masses, while MEMR2 is fit to the meteor-derived mass flux for higher masses. In the meteor range our flux sits between these two models. However, our flux has not been scaled to measured flux at the Earth.

Additionally, we examine the flux and mean impact speed at objects on circular orbits at different radial distances in the range of 0.1–5 AU (Fig. 15). The flux of modelled 10^{-6} g (~50 μm) meteoroids does not follow the radial behaviour of the flux of similar-sized IMEM meteoroids: this radial profile is first observed for 12.5–25 μm particles. The radial profile of the IMEM model at these sizes is based on Helios zodiacal light observation, for which it was assumed that the mass flux at Earth from Grün et al. (1985) was valid also at smaller radial distances. However, our model suggests that the mass distribution may vary with radial distance: the cross-sectional area peaks for particles with radii of 50 μm at Earth, but for particles with radii of 12.5 μm at 0.2 AU from the Sun.

Figure 16 additionally demonstrates that while the dust density of 250 μm particles is dominated by JFC meteoroids at the Earth (~95%), the asteroidal population reaches about 50% of the total dust density in the asteroid belt. This relative increase in the asteroidal component is only seen for larger particles. The contribution of different source populations to the total dust cloud is also a function of particle size. At the Earth, the contributions for JFC, HTC, and AST meteoroids varies from [90.9% 0.8% 8.3%] for 1 μm particles to [97.7% 0.5% 1.8%] for 250 μm, and remains at this level for higher masses.

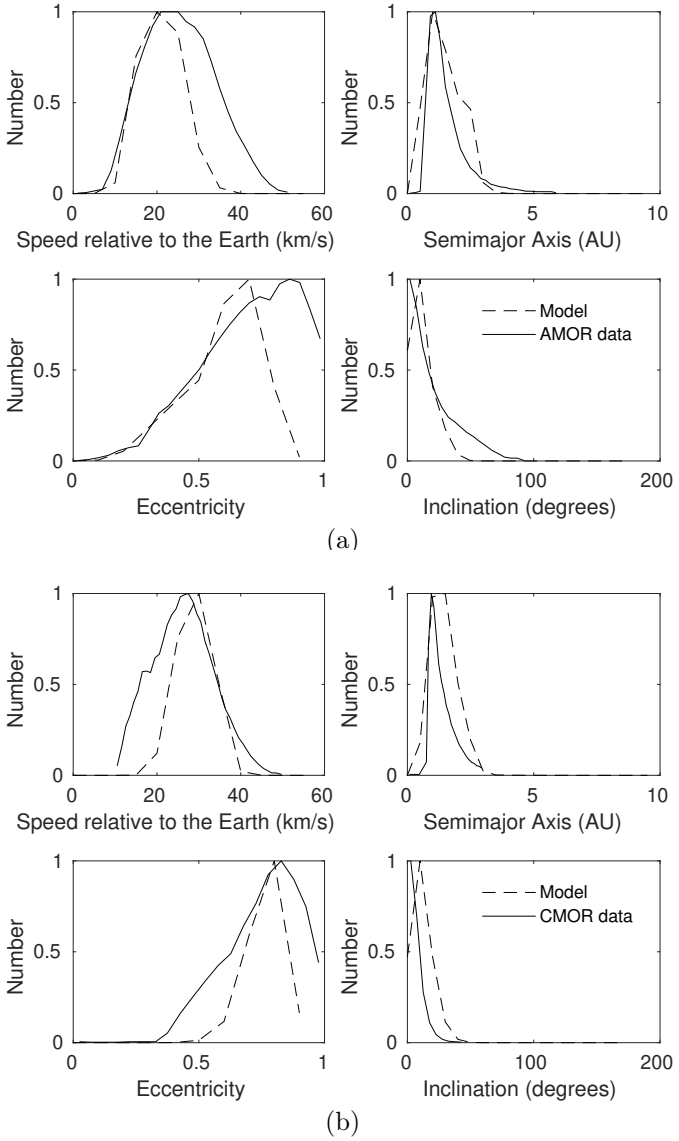

Fig. 12. Modelled impact speed and orbital elements at Earth for the helion meteor category with the ionization limit set for the AMOR (*a*) and CMOR (*b*) systems. The population weighting are derived from the infrared data (see Fig. 11). Population weighting 80%JFC, 0.5% HTC, 19.5% AST. $F_{\rm coll}$ = [1 1 1 1 1 1 50 50 50 50 50 50]. Mass distribution $\alpha = 5, \beta = 2$, $D_{\rm mid} = 150\ \mu$m.

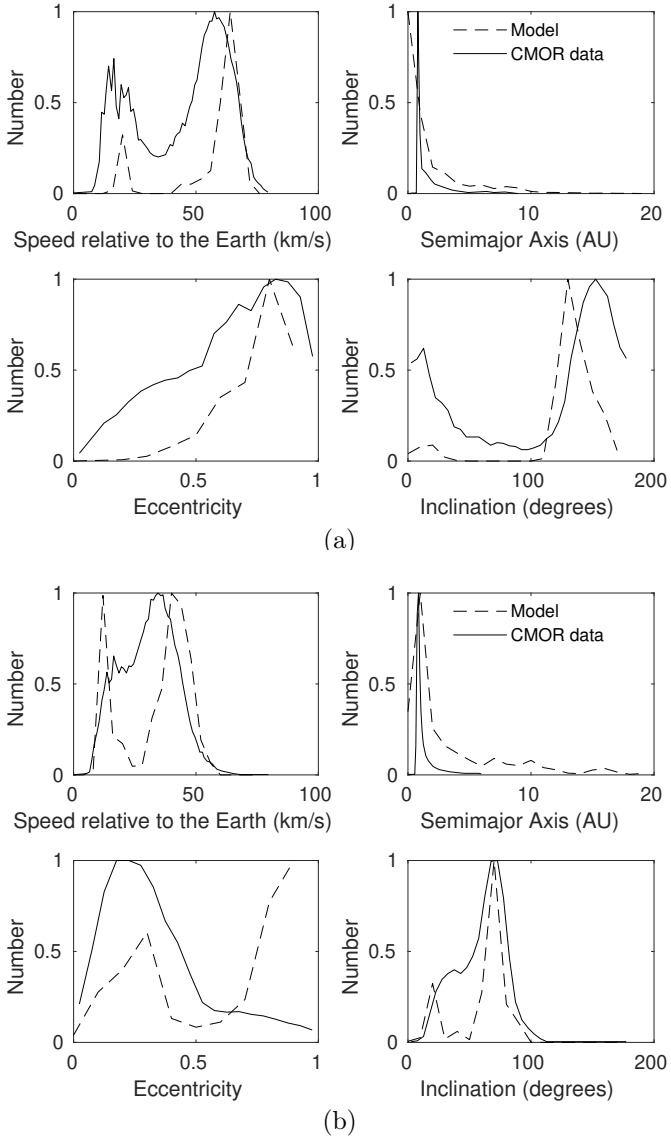

Fig. 13. Modelled impact speed and orbital elements at Earth for the apex (*a*) and toroidal meteor category (*b*), with the population weighting derived from the infrared data (see Fig. 11). Population weighting 80% JFC, 0.5% HTC, and 19.5% JFC. $F_{\rm coll}$ = [1 1 1 1 1 1 50 50 50 50 50 50]. Mass distribution $\alpha = 5, \beta = 2$, $D_{\rm mid} = 150\ \mu$m.

5. Discussion

The model provides a picture of the interplanetary dust cloud that is able to describe various observational datasets. Here we discuss the consequences of the final choice of parameters, the effect of assumptions made in developing this dust model, and potential further improvements and extensions of this model.

Our choice of $F_{\rm coll}$ = [1 1 1 1 1 1 50 50 50 50 50 50] is only a first approximation. Likely, there is a smooth transition between the collisional behaviour of small and larger particles. However, the datasets we have only provide evidence for two "regimes". As discussed above, it is also possible that $F_{\rm coll} < 1$ is required for some particle sizes. This however creates problems for the lunar microcrater distribution and increases the ratio between the modelled and measured flux at Earth. However, the Γ factor used for the collisional lifetime calculations is highly uncertain and valid only for crystalline rock. Meteoroids have likely different

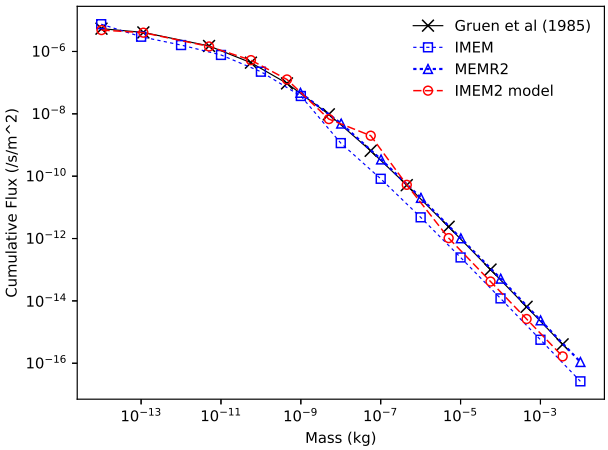

Fig. 14. Modelled IMEM2 flux (corrected for flux on a flat plate) compared to the flux from IMEM, MEMR2, and Grün et al. (1985).

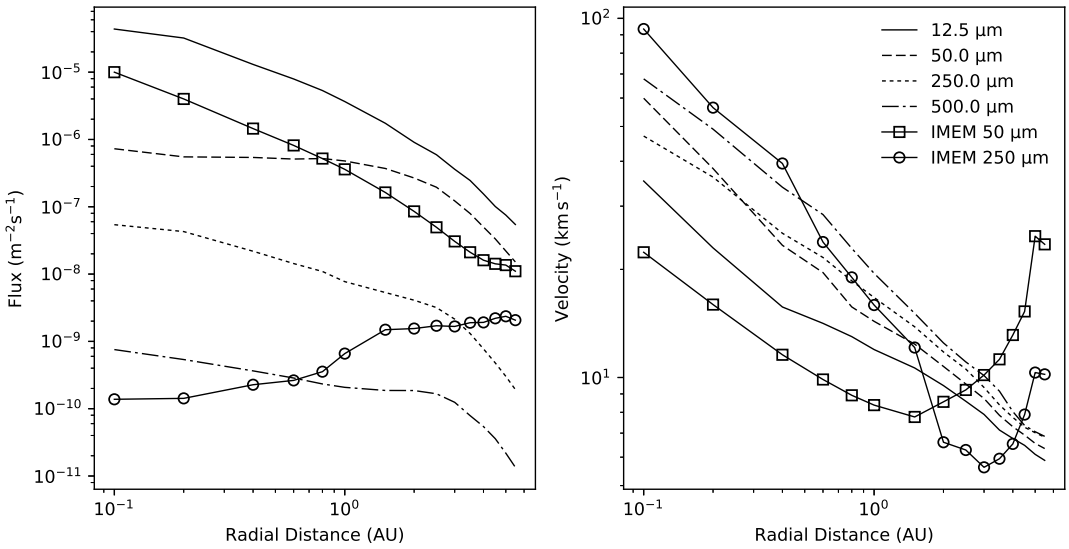

Fig. 15. Flux and impact speed at objects on circular orbits at different radial distances for different particle sizes, compared to flux and impact speed from IMEM. Impact speeds for modelled particles with radii >500 μm do not vary significantly. Modelled flux for particles with radii >500 μm is similar in shape but lower than the 500 μm flux.

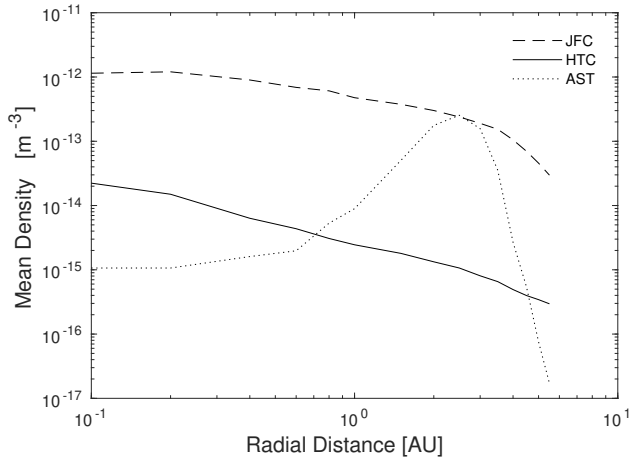

Fig. 16. Density variation for 250 μm particles with radial distance for the JFC, HTC, and AST populations.

composition and structural properties that are not fully considered in this model. For example, as described above, the porosity of the material will have a significant effect on the collisional behaviour.

Our use of crater flux measurements means that the size distribution of emitted particles is chosen such that the dust cloud accurately describes the observed crater size distribution of Grün et al. (1985). However, this distribution varies from differential size distributions derived from cometary trail observations: for example, modelling of the dust emission of 67P/Churyumov-Gerasimenko by Agarwal et al. (2010) to match *Spitzer* infrared observations of the trail requires $D_{\rm mid} \approx 2$ μm, $\alpha = 3.7$, and $\beta = 1.8$. Measurements at this comet suggest similar slopes, but a different knee of the distribution: Rotundi et al. (2015) report a size distribution from the GIADA instrument with a slope of -4 for particles >1 mm and a slope of -2 for smaller particles. However, Fulle et al. (2016) report that the size distribution of dust emitted by 67P/Chruyumov-Gerasimenko also varies with heliocentric distance. We also considered a variation in the size distribution for the cometary and asteroidal populations. However, a flatter distribution in the AST source lead to incompatible flux distributions because the asteroidal component was then dominant at larger particle sizes and was several orders of magnitude above the Grün et al. (1985) flux.

The bulk density is also uncertain. We used different values for different populations. Our choice of HTC and AST bulk densities of 1000 and 4000 kg m^{-3} is motivated by the meteor-derived number densities of Kikwaya et al. (2011). Moorhead et al. (2017) expand on this to develop a two-population density model for meteoroids, consisting of two probability distributions centred on ~1000 and ~4000 kg m^{-3}. We however chose 2000 kg m^{-3} for JFCs. This is partially to ensure this crucial component evolves sufficiently within the 1 Myr time-frame, but is also more consistent with other studies (Close et al. 2012). However, the bulk density is not a strong factor in the particle dynamics. Tests with bulk densities of JFC particles with 2000 and 4000 kg m^{-3} provided very similar results to those of the final model.

Our population weighting factors propose that, within the field of view of the COBE observations, the interplanetary dust cloud contains a large proportion (20%) of asteroidal dust, very little HTC dust (0.5%), and a dominant component (80%) of JFC dust. This is in contrast to the larger JFC component to the infrared brightness concluded by Nesvorný et al. (2010) (85–95%). Additionally, using infrared data Rowan-Robinson & May (2013) find that the interplanetary dust in the inner solar system is 70% cometary, 22% asteroidal, and 7.5% interstellar. However, in our model the contribution of JFC meteoroids to the spatial density of interplanetary dust particles at the Earth is higher (90–98%).

There are two components of these previous models that we do not consider here: interstellar dust and asteroidal dust bands. The former is likely only important for very small particles and a significant contribution of larger (>10 μm) particles is not expected as a result of the mass distribution (Krüger et al. 2015). The latter is likely only a small contribution at the Earth, but may be a signficant contributor in the asteroid belt (Nesvorný et al. 2010). A thorough model of the asteroid dust bands was outside the scope of this current project. However, it is not likely to significantly change our results as the asteroid bands are only

observable as a very small contributor to the infrared brightness and asteroidal particles are not easily observable as meteors at the Earth as a result of their low speeds. Furthermore, our population weightings are derived from COBE data, where the dominant particle size is in the range of 30–50 μm. These results are therefore scaled to a limited particle-size regime and are therefore dependent on the mass distribution.

We have also not included a specific Encke-type comet source. The Encke-type comets are much less numerous than JFCs, accounting for 52 objects in the JPL small body database (as of November 2017), compared to 645 JFCs. These objects need long timeframes to reach orbits interior to Jupiter and are likely to be dynamically old and exhausted of much of their ices (Levison et al. 2006b). However, 2P/Encke itself is thought to be a major contributor to the interplanetary dust cloud and perhaps the origin of observed asymmetries in the helion and antihelion categories (Wiegert et al. 2009). Such asymmetries are also imperceptible from our rotationally symmetric model. We tested a simple Encke-type source using the semi–major axis and eccentricity distribution of Levison et al. (2006b) and fitting the inclination distribution to the inclinations of observed Encke-type comets. The results are very similar to the JFC meteoroids for the meteor radar data, but similar to the AST source for the infrared data on account of their low inclinations. However, as a result of uncertainty surrounding their ability to be dynamically old and strong contributors to the dust cloud, and because we do not have sufficient orbital data to separate them from other sources, we excluded them from the final analysis.

There are also further observational datasets that would provide useful information for the model. In situ spacecraft data can constrain the flux of smaller meteoroids (~1–5 μm) away from the orbit of Earth. There are new sources of meteor orbital information that could be included (e.g. SAAMER, Janches et al. 2015 and CAMS, Jenniskens et al. 2016). Additionally, the proportion of meteors in different meteor radiant categories (helion/apex/toroidal) can provide information on the proportion of JFC and HTC particles. Longer integrations would be required to describe the HTC-component of the apex and toroidal categories.

The restriction of the particle integration to 1 Myr is one of the major limitations of the model. As a consequence, our simulations have partially insufficent orbital evolution of, in particular, the HTC and asteroidal sources. The JFC particles are also affected at smaller sizes: 25, 250, and 2500 μm particles start with average collisional lifetimes of 4×10^5, 2×10^5, and 7×10^4 yr, respectively. This can also affect larger particles, for which the collisional lifetimes are again larger (Fig. 1). They would therefore also benefit from individual integration, rather than having their dynamics based on 1.25 mm particles as described in Sect. 2. The 1 Myr integration time will therefore limit the circularisation of the JFC and HTC sources and the inspiralling of AST particles to the Sun, both as a consequence of PR drag.

The model is a first step at building a comprehensive meteoroid model from the ground up, using a number of different datasets to constrain parameters. The following are the further steps towards a model that fully describes the interplanetary dust cloud and uses all available observational datasets:

– Further iterations of the collision model are required, including fragmentation and updating the base interplanetary impactor model.

– Longer-term integrations over 5–10 million years are needed in order to improve the fit of HTC to meteor observations and the inspiralling of the asteroidal components.

– Additional populations are needed, such as Encke-type comets, near-Earth asteroids, asteroid dust bands, Oort-cloud comets, and the interstellar dust contribution.

– Additional datasets are needed, such as in situ data and additional meteor orbit data, as well as use of the relative strength of different meteor sporadic sources/categories to constrain the population weightings.

– The effects of variation of particle properties such as porosity on the particle dynamics and collisional behaviour should also be considered.

– Finally, further tests are required in order to see whether the above changes can improve the observational fits.

6. Conclusions

We integrated meteoroids released from source cometary and asteroidal meteoroid populations over 1 Myr in order to develop a dynamical model of the interplanetary dust cloud, which also contains a simple implementation of catastrophic collisions. The final dust cloud contains 1 μm–1 cm particles from Jupiter-family and Halley-type comets, and main belt asteroids. Collisional parameters, mass distribution, and scaling to absolute particle numbers were fit using COBE infrared brightness data, lunar microcrater diameter information, and meteor orbital and velocity observations. These observational data sets have different sensitivities to different particle sizes where COBE and meteor observations refer to larger particle sizes, whereas the lunar craters comprise the whole size regime. We are able to fit most observations, and the absolute scaling to COBE data leads to a flux at the Earth that is a good match to the Pegasus measurement and is largely within a factor of approximately two of the meteor observations in the orbit of Earth. The result is a dynamical meteoroid engineering model that represents a significant advancement of the current ESA IMEM model.

Our model allows us to draw the following conclusions. Firstly, large particles ($\gtrsim$200 μm) require longer collisional lifetimes than those reported by Grün et al. (1985), while smaller particles demand no such enhancement. This is confirmation of the results of Nesvorný et al. (2010, 2011a) and Pokorný et al. (2014), and will have implications for the collisional balance and the particle sizes for which collisional or Poynting-Robertson drag are dominant in their evolution. Furthermore, the model suggests a role for porosity in particle evolution.

Secondly, our model agrees with the results of Nesvorný et al. (2010) suggesting that the dust cloud at the Earth is dominated by JFC meteoroids (>90%), although we required a smaller (~80%) contribution to match 25 μm COBE data. Nevertheless, our results may still underestimate the fraction of asteroidal dust entering the atmosphere of Earth, as the low-velocity asteroidal component can be more strongly focussed and also more prone to capture in near-Earth resonances (Kortenkamp 2013).

In addition to the further steps towards a more comprehensive model, listed in Sect. 5, the development of such dust environment models would benefit significantly from the collection of data on the meteoroid population away from the Earth, such as information on meteors at Mars and Venus; infrared brightness observations of the dust cloud away from 1 AU; and in situ detection of large (>100 μm) particles also away from the vicinity of the Earth. Such information would constrain the flux as a function of radial distance.

Acknowledgements. This work is funded under ESA contract 4000114513/15/NL/HK. This research has made use of data provided by the International Astronomical Union's Minor Planet Center.

References

Agarwal, J., Müller, M., Reach, W. T., et al. 2010, Icarus, 207, 992
Berg, O. E., & Gerloff, U. 1971, Space Research XI, eds. K. Y. Kondratyev, M. J. Rycroft, & C. Sagan (Berlin: Akademie Verlag), 225
Berg, O. E., & Richardson, F. F. 1969, Rev. Sci. Instrum., 40, 1333
Borin, P., Cremonese, G., Marzari, F., Martellato, E., & Bruno, M. 2011, in EPSC-DPS Joint Meeting 2011, 455
Campbell-Brown, M. D. 2008, Icarus, 196, 144
Close, S., Volz, R., Loveland, R., et al. 2012, Icarus, 221, 300
Cour-Palais, B. G. 1969, Meteoroid Environment Model-1969: Near Earth to Lunar Surface, NASA SP-8013 (Washington, DC: NASA)
Dikarev, V., Grün, E., Baggaley, J., et al. 2005, Adv. Space Res., 35, 1282
Divine, N. 1993, J. Geophys. Res., 98, 17029
Dormand, J. R., & Prince, P. J. 1978, Celest. Mech., 18, 223
Fienga, A., Manche, H., Laskar, J., & Gastineau, M. 2008, A&A, 477, 315
Fienga, A., Laskar, J., Morley, T., et al. 2009, A&A, 507, 1675
Fienga, A., Laskar, J., Kuchynka, P., et al. 2010, IAU Symp. 261, 159
Fienga, A., Laskar, J., Manche, H., et al. 2011, Celest. Mech. Dyn. Astron., 111, 363
Fienga, A., Manche, H., Laskar, J., Gastineau, M., & Verma, A. 2014, ArXiv e-prints [arXiv:1405.0484]
Fienga, A., Laskar, J., Exertier, P., Manche, H., & Gastineau, M. 2015, Celest. Mech. Dyn. Astron., 123, 325
Folkner, W. M., Williams, J. G., Boggs, D. H., Park, R. S., & Kuchynka, P. 2014, Interplanet. Netw. Prog. Rep., 196, C1
Fulle, M., Marzari, F., Della Corte, V., et al. 2016, ApJ, 821, 19
Galligan, D. P., & Baggaley, W. J. 2005, MNRAS, 359, 551
Gault, D. E. 1973, Moon, 6, 32
Gladman, B. J., Davis, D. R., Neese, C., et al. 2009, Icarus, 202, 104
Gruen, E., Pailer, N., Fechtig, H., & Kissel, J. 1980, Planet. Space Sci., 28, 333
Grün, E., Zook, H. A., Fechtig, H., & Giese, R. H. 1985, Icarus, 62, 244
Grün, E., Baguhl, M., Divine, N., et al. 1995a, Planet. Space Sci., 43, 953
Grün, E., Baguhl, M., Divine, N., et al. 1995b, Planet. Space Sci., 43, 971
Hawkins, G. S. 1956, AJ, 61, 386
Hawkins, G. S. 1962, AJ, 67, 241
Hawkins, G. S. 1963, Smithson. Contrib. Astrophys., 7, 53
Hoerz, F., Morrison, D. A., Brownlee, D. E., et al. 1975a, Planet. Space Sci., 23, 151
Hoerz, F., Schneider, E., Gault, D. E., Hartung, J. B., & Brownlee, D. E. 1975b, Moon, 13, 235
Hoffmann, H.-J., Fechtig, H., Gruen, E., & Kissel, J. 1975a, Planet. Space Sci., 23, 215
Hoffmann, H.-J., Fechtig, H., Gruen, E., & Kissel, J. 1975b, Planet. Space Sci., 23, 985
Janches, D., Close, S., Hormaechea, J. L., et al. 2015, ApJ, 809, 36
Jenniskens, P., Nénon, Q., Gural, P. S., et al. 2016, Icarus, 266, 384
Jones, J., & Brown, P. 1993, MNRAS, 265, 524
Kelsall, T., Weiland, J. L., Franz, B. A., et al. 1998, ApJ, 508, 44
Kessler, D. J. 1970, Meteoroid Environment Model-1970: Interplanetary and Planetary, NASA SP-8038 (Washington, DC: NASA)
Kikwaya, J.-B., Campbell-Brown, M., & Brown, P. G. 2011, A&A, 530, A113
Kortenkamp, S. J. 2013, Icarus, 226, 1550
Koschny, D., Drolshagen, E., Drolshagen, S., et al. 2017, Planet. Space Sci., 143, 230
Krüger, H., Strub, P., Grün, E., & Sterken, V. J. 2015, ApJ, 812, 139
Levison, H. F., & Duncan, M. J. 1997, Icarus, 127, 13
Levison, H. F., Duncan, M. J., Dones, L., & Gladman, B. J. 2006a, Icarus, 184, 619
Levison, H. F., Terrell, D., Wiegert, P. A., Dones, L., & Duncan, M. J. 2006b, Icarus, 182, 161
Love, S. G., & Brownlee, D. E. 1993, Science, 262, 550
Love, S. G., Hörz, F., & Brownlee, D. E. 1993, Icarus, 105, 216
Mann, I., Pellinen-Wannberg, A., Murad, E., et al. 2011, Space Sci. Rev., 161, 1
McNamara, H., Jones, J., Kauffman, B., et al. 2004, Earth Moon Planets, 95, 123
Moorhead, A. V., Koehler, H. M., & Cooke, W. J. 2015, NASA Meteoroid Engineering Model Release 2.0, NASA/TM-2015-218214
Moorhead, A. V., Blaauw, R. C., Moser, D. E., et al. 2017, MNRAS, 472, 3833
Morrison, D. A., & Clanton, U. S. 1979, Lunar Planet. Sci. Conf. Proc., 10, 1649
Moyer, T. 1971, DPODP Manual, IOM 3215-37, JPL
Nakamura, A. M., Fujiwara, A., Kadono, T., & Shirono, S. 1994, in 75 Years of Hirayama Asteroid Families: The Role of Collisions in the Solar System History, eds. Y. Kozai, R. P. Binzel, & T. Hirayama, ASP Conf. Ser., 63, 237
Nakamura, A. M., Yamane, F., Okamoto, T., & Takasawa, S. 2015, Planet. Space Sci., 107, 45
Naumann, R. J. 1966, The Near-Earth Meteoroid Environment, NASA Technical Note (NASA TN D-3717)
Nesvorný, D., Jenniskens, P., Levison, H. F., et al. 2010, ApJ, 713, 816
Nesvorný, D., Janches, D., Vokrouhlický, D., et al. 2011a, ApJ, 743, 129
Nesvorný, D., Vokrouhlický, D., Pokorný, P., & Janches, D. 2011b, ApJ, 743, 37
Pokorný, P., Vokrouhlický, D., Nesvorný, D., Campbell-Brown, M., & Brown, P. 2014, ApJ, 789, 25
Rotundi, A., Sierks, H., Della Corte, V., et al. 2015, Science, 347, 3905
Rowan-Robinson, M., & May, B. 2013, MNRAS, 429, 2894
Soja, R. H., Sommer, M., Herzog, J., et al. 2015, A&A, 583, A18
Staubach, P., Grün, E., & Jehn, R. 1997, Adv. Space Res., 19, 301
Sykes, M. V., Grün, E., Reach, W. T., & Jenniskens, P. 2004, Comets II, eds. M. C. Festou, H. U. Keller, & H. A. Weaver (Tucson, AZ: University of Arizona Press), 677
Verniani, F. 1965, Smithson. Contrib. Astrophys., 8, 141
Viswanathan, V., Fienga, A., Minazzoli, O., et al. 2018, MNRAS, 476, 1877
Weiss, A. A., & Smith, J. W. 1960, MNRAS, 121, 5
Weryk, R. J., & Brown, P. G. 2013, Planet. Space Sci., 81, 32
Wiegert, P., Vaubaillon, J., & Campbell-Brown, M. 2009, Icarus, 201, 295